Eigenmode Tomography of Surface Charge Oscillations of Plasmonic Nanoparticles by Electron Energy Loss Spectroscopy

Sean M. Collins,[*,†] Emilie Ringe,[‡] Martial Duchamp,[§] Zineb Saghi,[†] Rafal E. Dunin-Borkowski,[§] and Paul A. Midgley[*,†]
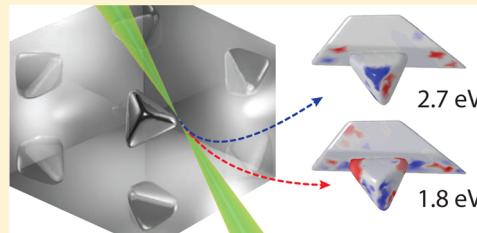
[†]Department of Materials Science and Metallurgy, University of Cambridge, 27 Charles Babbage Road, Cambridge, CB3 0FS, United Kingdom

[‡]Department of Materials Science and Nanoengineering, Rice University, 6100 Main Street MS-325, Houston, Texas 77005-1827, United States

[§]Ernst Ruska-Centre for Microscopy and Spectroscopy with Electrons and Peter Grünberg Institute, Forschungszentrum Jülich, D-52425 Jülich, Germany

S *Supporting Information*

ABSTRACT: Plasmonic devices designed in three dimensions enable careful tuning of optical responses for control of complex electromagnetic interactions on the nanoscale. Probing the fundamental characteristics of the constituent nanoparticle building blocks is, however, often constrained by diffraction-limited spatial resolution in optical spectroscopy. Electron microscopy techniques, including electron energy loss spectroscopy (EELS), have recently been developed to image surface plasmon resonances qualitatively at the nanoscale in three dimensions using tomographic reconstruction techniques. Here, we present an experimental realization of a distinct method that uses direct analysis of modal surface charge distributions to reconstruct quantitatively the three-dimensional eigenmodes of a silver right bipyramid on a metal oxide substrate. This eigenmode tomography removes ambiguity in two-dimensional imaging of spatially localized plasmonic resonances, reveals substrate-induced mode degeneracy breaking in the bipyramid, and enables EELS for the analysis not of a particular electron-induced response but of the underlying geometric modes characteristic of particle surface plasmons.

KEYWORDS: surface plasmon, EELS, tomography, nanoparticles

Single particle surface plasmon resonances have been the focus of intense investigation for an increasingly broad range of applications from biological and chemical sensing[1,2] to waveguiding and metamaterials[3] to solar energy conversion and storage.[4] Such single-particle plasmonic behavior forms the basis for coupled[5] and periodic systems where individual particle resonances combine according to principles of mode hybridization.[6] Studies of plasmonic metal nanocubes,[7−9] triangular prisms,[10] and nanorods[11] have constituted the prototypical cases for identifying principles of plasmonic mode structure, substrate and interparticle coupling effects, and refractive index sensitivity. Diverse 3D nanocrystal morphologies have been reported including decahedra,[12,13] octahedra,[13] and right bipyramids,[14,15] but few comprehensive analyses of the available multipolar modes have been performed.[12] These particles offer specific control over spatially localized excitations due to the reduced symmetry of their geometries and are competitive candidates for optimized sensing[16] and solar energy applications.[17]

Understanding the relationship between nanoparticle geometry and plasmonic response has been augmented by significant electron microscopy advances in the subdiffraction-limited investigation of plasmonic nanoparticles by correlative optical microscopy,[13] tomography of particle morphology,[18,19] and monochromated EELS of both optically "bright" and "dark" resonances.[10,11] For quasi-two-dimensional nanoparticles, the EELS signal is related to a localized density of states (LDOS).[20] However, the LDOS interpretation of EELS cannot be generalized for arbitrary geometries, although in the quasi-static approximation an EELS map bears resemblance to the potential in the vicinity of the nanoparticle.[21−23] Moreover, EELS observations across a range of specimen tilt angles are increasingly necessary for unambiguous measurement of plasmon resonances in single particles[22,24−26] and multiparticle devices.[27] Here, surface charge tomography of low-symmetry silver bipyramids on MoO_3, a 2D semiconductor and sensor material and a common solar cell component,[17] serves as a model analysis for experimental 3D measurement of the optical response characteristics of arbitrary geometries in realistic plasmonic technologies.

The principles of surface charge tomography of plasmonic eigenmodes rely on the quasi-static formulation for the energy loss probability Γ^{EELS} given as a sum over eigenmodes:[23,28]
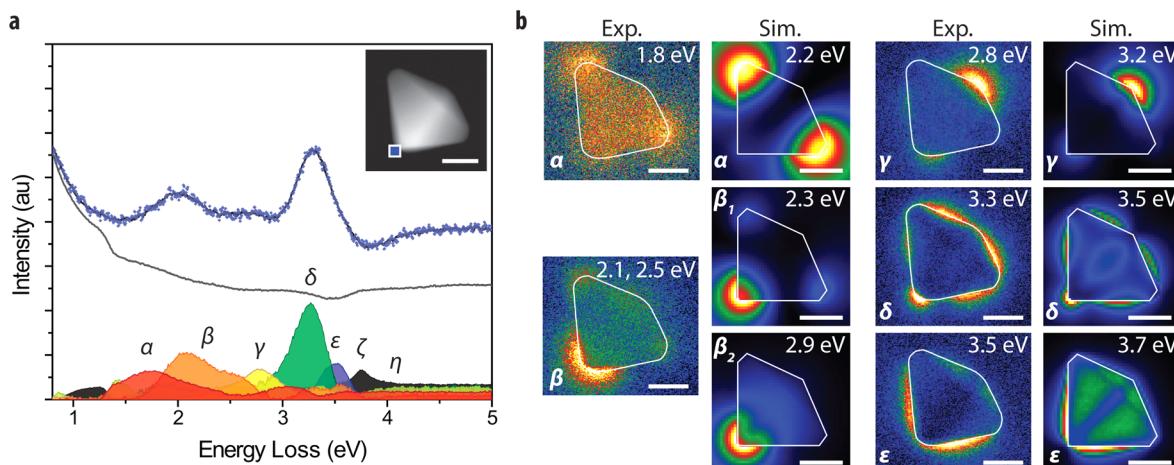
Figure 1. Plan-view EELS spectrum imaging of a silver right bipyramid. (a) Non-negative matrix factorization (NMF) of EELS for a selected area (blue square, inset). The decomposition is shown for a 4.3 nm × 4.3 nm (9 pixel × 9 pixel) region. Blue dots represent the summed raw spectra, the black line is the sum of all decomposition components, the gray line corresponds to the spectral signature of the zero loss peak (ZLP), and each of the remaining components corresponds to a spatial map that exhibits a dominant contribution matching a surface plasmon mode of the bipyramid ($\alpha-\varepsilon$), the bulk plasmon (ζ), or the MoO_3 substrate band edge (η). (b) NMF component maps (Exp.) and simulated energy loss probability maps (Sim.). Intensities are plotted on a normalized scale for each map. Subscripts on β denote fully resolved peaks in simulated spectra represented in the single experimental NMF component β. Energies refer to peak maxima in the respective experimental and simulated spectra. Scale bars are 25 nm.

$$\Gamma^{EELS}(\mathbf{R}_0, \omega) = \sum_k A_k(\omega) \left| \oint d\mathbf{s}\, \phi^*_{\mathbf{R}_0}(\mathbf{s})\, \sigma_k(\mathbf{s}) \right|^2 \tag{1}$$

where the integral is over the surface differential $d\mathbf{s}$, $\phi_{\mathbf{R}_0}(\mathbf{s})$ is the potential of the exciting electron traveling along a trajectory defined in the plane perpendicular to the trajectory by the coordinate $\mathbf{R}_0$, $\sigma_k(\mathbf{s})$ is the surface charge along the surface $\mathbf{s}$, and $A_k(\omega)$ is a frequency-dependent coefficient for eigenmode k. The quasi-static approximation applies strictly only in the small-particle limit, as a complete electrodynamic description (i.e., with retardation effects) includes surface currents in addition to surface charges. However, the surface plasmon response is well described by the surface charge eigenmodes even for particle sizes exhibiting noticeable retardation effects (see Figure S5), and near-field behavior is quantitatively similar for the quasi-static and fully retarded cases for particles up to 50 nm in size (Figure S6).

For a particular trajectory and corresponding pixel in the spectrum image n, a cost function minimization problem can be defined as

$$\hat{\sigma} = \arg\min_{\hat{\sigma}} \{ \| \Gamma_n^{exp}(\hat{\sigma}) - \Gamma_n^{calc}(\hat{\sigma}) \|_2^2 \} \tag{2}$$

to identify the surface charge vector $\hat{\sigma}$ that minimizes the ℓ_2-norm of the difference between experimental and calculated loss probabilities at fixed ω at the resonant frequency of a single mode k. The subscript notation in eq 2 refers to the ℓ_2-norm, defined as $\|\hat{x}\|_2 = (\sum_i |x_i|^2)^{1/2}$ for any vector $\hat{x}$ with elements x_i. Notably, eq 1 is correct for nonpenetrating trajectories only. Experimental realization poses significant challenges particularly in separating intrinsically overlapping or experimentally unresolved spectral peaks, accurately defining the experimental particle surface, and in recording signals of sufficient quality and self-consistency throughout the data-acquisition time. Progress in applying multivariate decomposition approaches such as non-negative matrix factorization (NMF)[22] and electron tomography techniques using compressed sensing[29] enables modal peak separation and high-quality surface reconstructions

from limited tilt-series data sets. Contamination by carbon deposition under the electron beam, however, presents an intrinsic limitation to the acquisition time of an EELS data set[22] and must be balanced with electron dose to maximize the signal-to-noise while minimizing beam exposure.

NMF decomposition and other multivariate analysis methods for separating multiple overlapping spectral components (spectral unmixing) have recently been applied to a number of examples in scanning transmission electron microscopy (STEM) EELS of particle surface plasmons,[22,30−33] but their use as input for a tomographic reconstruction of single particle plasmon modes merits a brief explanation. As given in eq 2, the tomographic problem requires input as a spatial probability map corresponding to a single plasmon mode. NMF decomposition separates experimental data into spectral components and associated intensity maps. The spectral components are often imperfect separations, although typically dominated by a single spectral feature. Moreover, the extent of imperfect separation is given by the residual spectral features away from the dominant peak feature. For a single plasmon mode k in eq 1, the eigenmode and its associated surface charge distribution is a purely geometric mode,[34] separable from the spectral energy dependence. The spatial intensity map becomes directly physically interpretable in this case. Experimentally, provided the spectral component can be identified with a particular dominant eigenmode or set of modes, the tomographic approach serves to reconstruct the energy-independent geometric eigen-charge distribution from the spatial intensity maps with minimal effects due to the residual spectral mixing.

Alternative approaches such as integrating over an energy window or fitting peaks could also be used to extract spatial intensity maps for input to surface charge reconstructions. While many methods introduce some bias (e.g., NMF requires the selection of an energy range for processing), integrating over an energy window or fitting peaks may incorporate undesirable bias in selecting the energy of the peak and choosing the number of peaks and may make assumptions about the shapes of the background and surface plasmon spectral signatures. Peak fitting approaches in principle enable
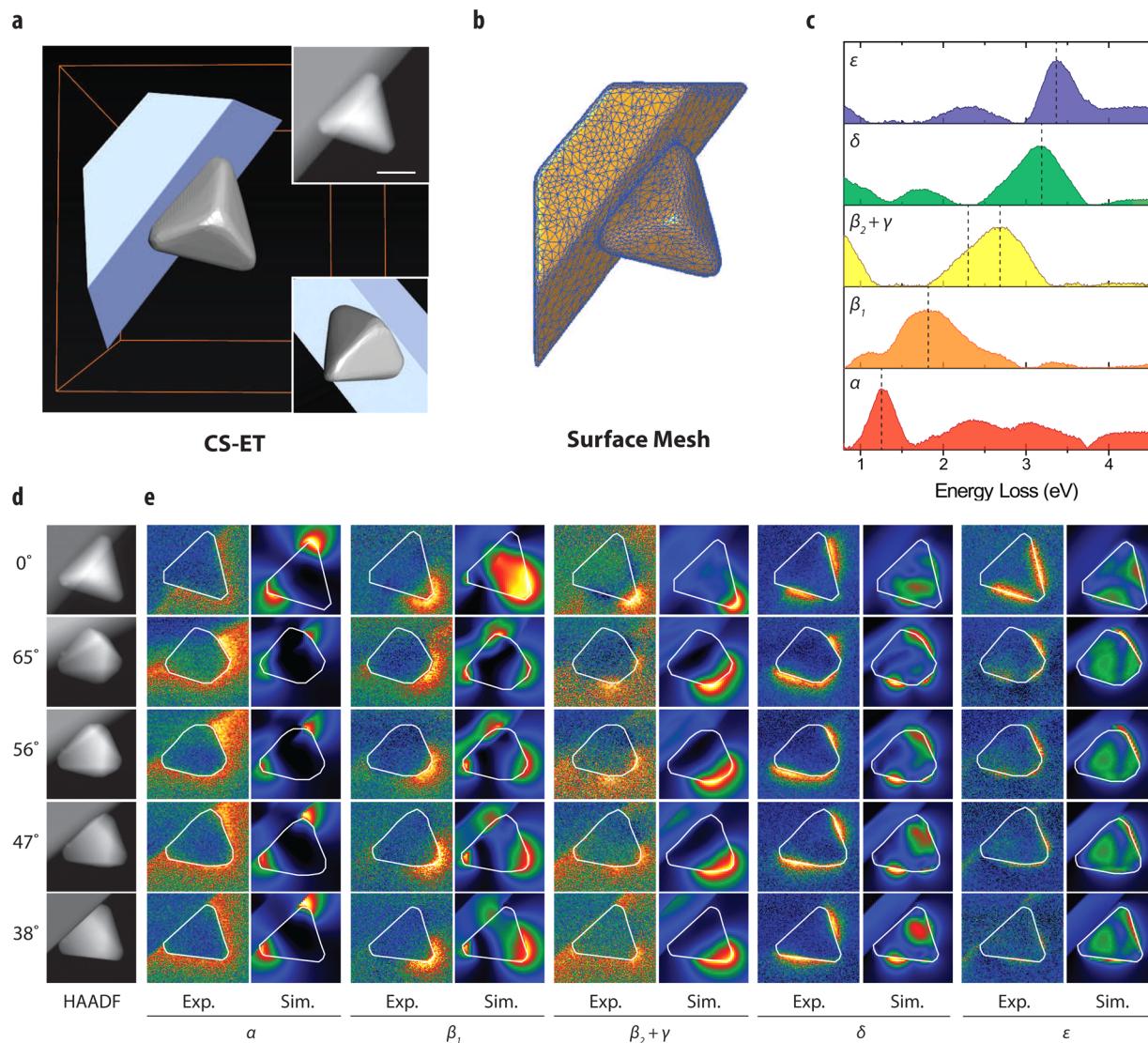
Figure 2. Electron tomography and tilt-series EELS of the surface plasmon modes of a silver right bipyramid on a MoO_3 substrate. (a) Surface representation of a compressed sensing electron tomography (CS-ET) reconstruction from tilt-series high angle annular dark field (HAADF) STEM. Insets show the 0° tilt HAADF micrograph and a plan-view perspective of the right bipyramid. The inset scale bar is 25 nm. (b) Surface mesh derived from the CS-ET reconstruction used for simulations in (e). (c) Spectral NMF decomposition factors for tilt-series EELS spectrum imaging corresponding to surface plasmon mode excitations of the bipyramid. Dashed vertical lines serve as a guide to the surface plasmon mode resonance energies. (d) HAADF micrographs at tilts recorded simultaneously with the EELS spectrum imaging. (e) Experimental NMF component maps and simulated loss probability maps at the corresponding tilt angles. Intensities are plotted on a normalized scale within each column. Greek letters denote spectral features and associated modal components as in Figure 1.

energy shifts in spectral peak positions to be recorded for well-known peak shapes. Such assumptions are complicated by the experimental spectral convolution with the poorly defined line shape associated with the initial spread of electron energies in the STEM probe, the zero loss peak (ZLP). Residual mixing in energy filtering or imperfect peak fitting will also be obscured in such approaches. Provided that NMF intensity maps are dominated by an identifiable number of individual surface plasmon modes, verifiable by comparison with simulations, the maps represent valid input for the tomographic reconstruction. The reconstruction will in turn be a quantitative representation of the dominant mode with an associated experimental uncertainty due to imperfect unmixing, noise, and other limits on precision.

Figure 1 presents an EELS analysis of a plan-view silver right bipyramid that highlights many of these key issues in 2D

spectrum imaging. The experimental data set was well described by decomposition into five surface plasmon features ($\alpha-\varepsilon$), the ZLP tail, the silver bulk plasmon (ζ), and the MoO_3 band edge (η) (see Figure S3). The β component, however, comprised two combined peaks in the spectral decomposition (Figure 1a). Boundary element method (BEM) simulations of the energy loss probability for an ideal bipyramid on a dielectric substrate ($n = 2.54$) revealed two peaks for the β component with maps exhibiting similar spatial intensity at the 90° corner of the plan-view bipyramid. NMF struggles to separate features when they exhibit such spectral and spatial similarity. Inspection of the unprocessed spectra along key trajectories supported the NMF decomposition and analysis of the β_1 and β_2 features (Figures S2, S5−S7). Retardation effects do not appear to signficantly affect the spectra for bipyramids of this size, resulting in a small red-shift in mode energies (Figure S5)

but negligible changes in the induced electric fields at the particle surface (Figure S6). The substrate likewise induces a shift in mode energies to lower energies relative to an isolated bipyramid but does not modify the number or character of the modes (Figure S7).

Since there are two corners aligned in projection at the 90° corner, the 3D localization of the source of the observed EELS signals remains ambiguous when only 2D data are considered. The simulated maps otherwise corresponded closely to the experimental decomposition maps. Imperfect separation of peaks by NMF appeared as small residual satellite peaks and an inflection in the ZLP tail near 1.4 eV, but these minor artifacts did not modify component maps significantly. Compared to simulations, the energies of experimental peaks were lower by 0.2−0.4 eV, a red-shift attributed to uncertainty in the substrate thickness and dielectric function and the local dielectric environment around the silver particle due to surfactant ligands or contamination. Additionally, the signal inside the particle was relatively weak due to the minimum dose beam conditions prioritizing nonpenetrating trajectories used experimentally. Plan-view EELS of another bipyramid is presented in Figure S4.

For 3D surface charge reconstructions using eq 1, truly nonpenetrating trajectories were obtained using an alternative cross-sectional sample orientation, shown in Figure 2 (inset). MoO_3 crystals were specifically selected for tomographic reconstruction purposes to enable the acquisition of EELS at trajectories passing through vacuum in accordance with the assumptions underpinning eq 1. Figure 2 presents a high angle annular dark field (HAADF) STEM tomography reconstruction of the surface of this silver bipyramid, the corresponding surface mesh generated for BEM simulations and surface charge reconstructions (Figure S8 presents simulated spectra), and the results of NMF decomposition including the spectral components, corresponding HAADF micrographs, and experimental NMF component and simulated loss probability maps. Figure 3 presents an overview of the processing steps involved for tomographic reconstruction (see also Methods). In brief, the presented method can be subdivided into acquisition, preprocessing, and reconstruction steps. The NMF decomposition presented in Figure 2 represents the EELS input for reconstruction. Throughout this multistep processing scheme, a number of alternative methods for intermediate steps might be considered, and several of these are emphasized in Figure 3, where the selected methods for analyzing the bipyramid are highlighted.

Spectrum images were acquired at high positive tilt angles to maximize the nonpenetrating trajectories available for reconstruction. Due to the buildup of carbon contamination, the first five spectrum images acquired were selected for EELS analysis (0°, 65°, 56°, 47°, and 38°). Spectrum images acquired at subsequent tilt angles exhibited significantly reduced signal across all modes and were therefore excluded from the analysis. Five NMF components were identified to describe the tilt-series EELS, and these components exhibited good correspondence with the six simulated features with the β_2 and γ spectral features unseparated by NMF (see Figure S11). Components were also extracted corresponding to the ZLP, bulk plasmon, and substrate components and a contamination-induced peak shift in the α component (Figures S12 and S13). For the α component the total signal was reduced at the first and final tilt angles due to this peak shift and damping resulting from carbon contamination. The associated spectral signature also shows a nonzero background intensity across a wide
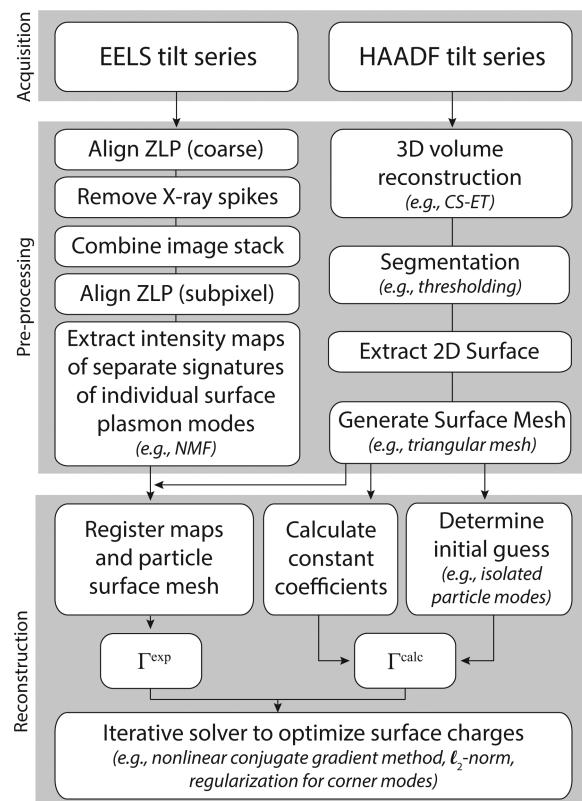
Figure 3. Summary of key processing steps in eigenmode tomography. Italics highlight the selected methods where alternatives might be considered.

spectral range, attributed to difficulties in extracting the relatively weak, damped signal localized predominantly in the substrate. The spectral component background varies slowly and consequently does not contribute sharp features to the recovered NMF map (Figure 2e). The asymmetric intensity at the two substrate-bound corners was preserved at high tilt, suggesting the NMF component map captures the experimental signal recovered for the mode expected from simulation. For the $\beta_2 + \gamma$ component, the angle-dependent intensity for each of the two "antinodes" reproduced the intensities in the simulated maps, confirming the NMF component is a sum of the β_2 and γ signatures. The greater spatial confinement for the β_2 signal suggests it is a higher order multipolar mode relative to β_1 and explains why the β_1 and β_2 signatures are separated by NMF when tilted away from the plan-view orientation. By comparing experimental and simulated signals for the particular tomographically reconstructed particle surface, these measurements present a complete mode analysis of a low-symmetry nanoparticle.

The origin of the spectral features observed in simulated and experimental maps can be understood in terms of the eigenmodes of an isolated right bipyramid depicted in Figure 4 (see Figure S14 for all eigenmode energies). Although these eigenmodes are defined in the quasi-static approximation, they provide a meaningful, physical description of the geometric modes underlying the optical response of the bipyramid. These modes can be categorized as corner, edge, and face modes according to the spectral and spatially mapped features observed in Figures 1 and 2. The corner modes are each identifiable as components α, β_1, β_2, and γ. The corner modes correspond to a doubly degenerate set of dipoles ($E'(x, y)$, (α,
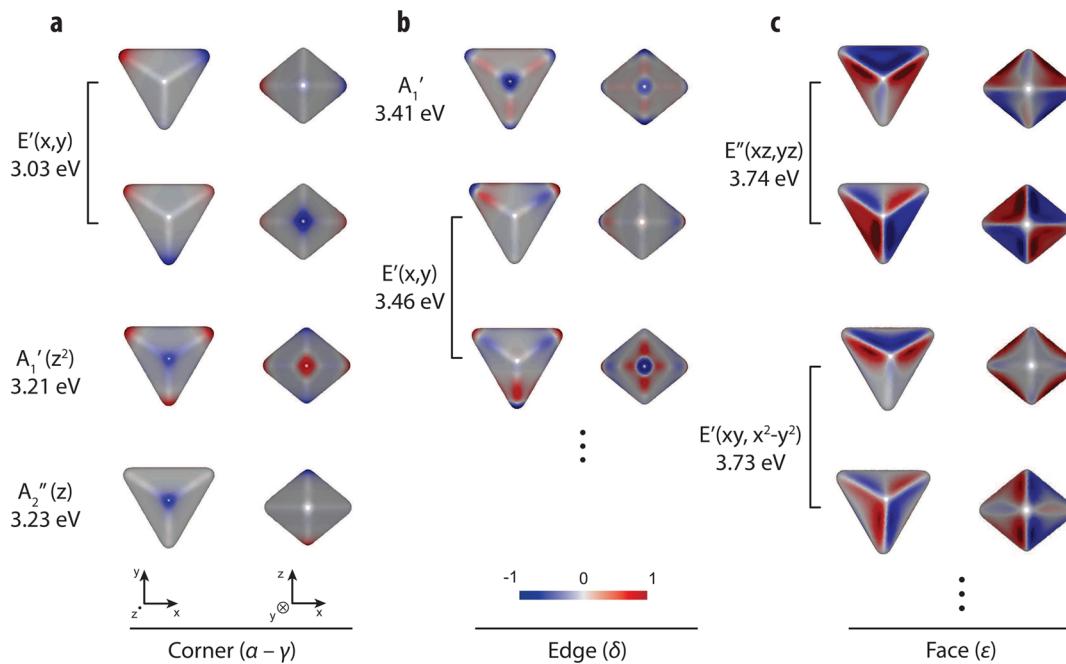
Figure 4. Surface charge distributions for principal eigenmodes of an isolated silver right bipyramid. (a) Corner modes corresponding to features α, β_1, β_2, and γ. (b) Lowest order multipolar modes in the series contributing to the edge mode feature δ. (c) Lowest order multipolar modes in the series contributing to the face mode feature ε. For each eigenmode, one orientation along the $C_3(z)$ axis of the bipyramid (left) and one perpendicular orientation (right) are shown corresponding to the indicated coordinate axes in (a). Symmetry labels are given in the D_{3h} point group, and brackets highlight degenerate pairs. Colors are shown on a normalized scale as shown. Eigenmode energies in the extended δ and ε series are plotted in Figure S14.
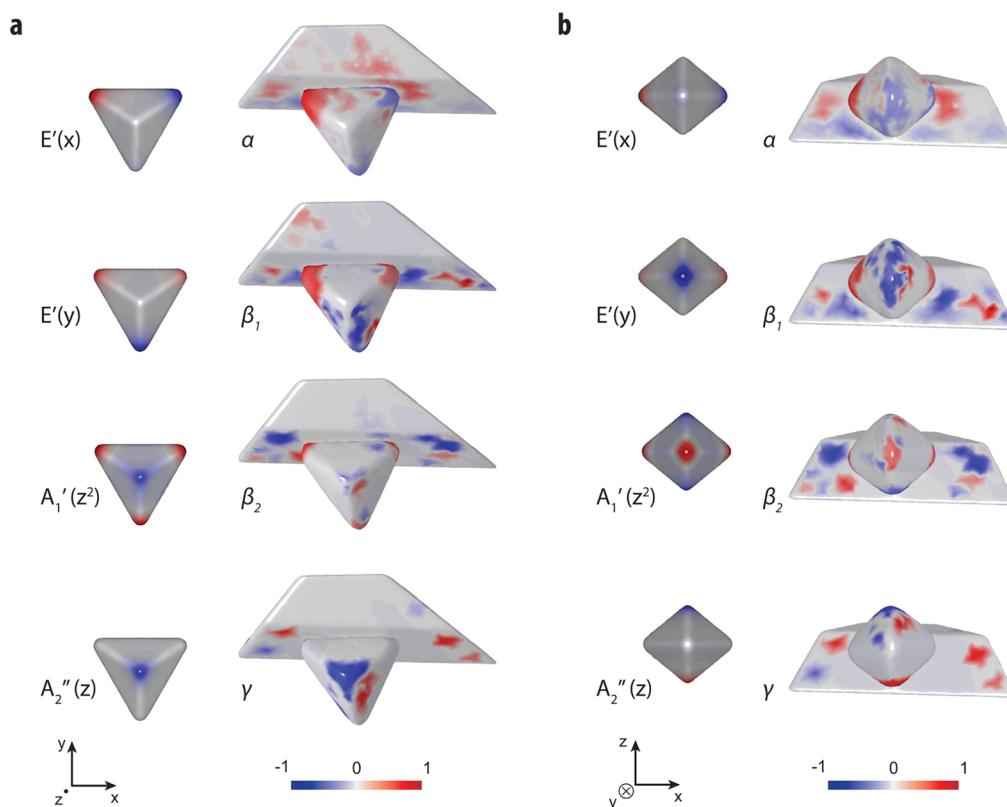
Figure 5. Corner eigenmodes and corresponding surface charge reconstructions for a silver right bipyramid on a MoO_3 dielectric substrate. (a, b) For each eigenmode, one orientation along the C_3 (z) axis of the bipyramid (a) and one perpendicular orientation (b) are shown corresponding to the indicated coordinate axes. The color scale is normalized for each mode. Greek letters refer to the corresponding spectral features as in Figures 1 and 2. Symmetry labels are given for an isolated bipyramd (D_{3h} point group).

β_1)) in the equatorial plane of the bipyramid perpendicular to the 3-fold rotation axis $C_3(z)$, an axial quadrupole ($A_1'(z^2)$, β_2), and an axial dipole ($A_2''(z)$, γ). As a consequence of substrate-induced symmetry breaking[9] in the experimental geometry, the equatorial dipole mode degeneracy is lifted and the x and y equatorial dipoles appear at different energies (α and β_1). The edge and face modes each comprise a series of higher order multipolar resonances, but each series is captured by a single spectral signature, δ and ε, respectively. Consequently, for the edge and face modes only the dominant contributions in the multipolar series can be recovered by reconstruction (see Figures S17–S20).

Figure 5 presents surface charge reconstructions of the corner modes, the principal dipolar and quadrupolar eigenmodes of interest for photonic applications. The surface charge units are plotted on a normalized scale due to the arbitrary scaling of NMF maps (see also Supporting Information). Due to the different local dielectric environment in the first and four subsequent tilts (Figure 2), only the four self-consistent maps from the NMF decomposition at 65–38° were employed for the reconstructions in Figure 5. In order to identify physical reconstructions in the context of experimental noise, eq 2 was modified to incorporate prior knowledge of the sparsity of eigenmode surface charge vectors in the form of a further regularization term (see Methods). This soft thresholding regularization term was tailored to reconstructions with highly localized surface charges, as in the case of the corner modes of the bipyramid. The reconstructions were further validated by examining recalculated EELS maps and residual differences between experimental maps and maps calculated from the reconstructed surface charge distributions (Figures S15 and S16). These calculations illustrate the role of precise image registration (see Figure 3), as residual differences are found predominantly in single-pixel discrepancies between the reconstructed surface and experimental EELS maps. The reconstruction algorithm was further tested in phantom calculations to demonstrate the significance of a reasonable initialization of the reconstruction (Figures S21–S23).

Complementary charges can be seen in the substrate, particularly for the α and β_1 reconstructions. The substrate charges far from the bipyramid for the α and β_2 components derive from the signal observed at the substrate–vacuum boundary in the tilt-series maps (Figure 2). The 3D surface charge reconstructions reveal that the x-dipole, localized predominantly in the substrate, occurs at lower energy than the y-dipole, with surface charge concentrated at the equatorial corner in vacuum. The EELS spectra and maps in Figure 2, clarified by the reconstructions in Figure 5, offer direct experimental evidence of this substrate-induced degeneracy breaking in the bipyramid.

We have established a practical tomographic method to reconstruct the 3D surface charge distributions of fundamental particle eigenmodes with nanometre spatial resolution. Analogous formulations to eq 1 for cathodoluminescence signals[35] suggest similar quantitative reconstruction methods are possible for electron-induced radiative emissions. Eigenmode tomography enables a precise optical analysis of single particles, particle ensembles, and plasmonic devices and offers a bridge between electron beam and near-field and far-field optical spectroscopy.

■ METHODS

Sample Preparation. Silver bipyramids were synthesized following a previously published synthesis.[36] In brief, a polyol reduction of silver nitrate ($AgNO_3$) was performed in ethylene glycol in the presence of poly(vinylpyrrolidone) and a small amount of sodium hydrosulfide (NaHS) under argon atmosphere. The reaction mixture was filtered to remove long rods, leaving cubes and bipyramids. Transmission electron microscope samples were prepared by depositing drops of silver nanoparticle solution on MoO_3 crystals dispersed on lacey carbon TEM grids (Agar Scientific).

Data Acquisition. STEM-EELS data were acquired using the FEI Titan 50-300 PICO equipped with an X-FEG electron gun and a Wien filter monochromator and operated at 300 kV. The beam convergence semiangle was 21.4 mrad. EELS spectra were acquired on a Gatan GIF Quantum ERS energy loss spectrometer with a dispersion of 0.005 eV per channel using a 260×2048 section of a 2048×2048 pixel charge-coupled device camera with a vertical binning of 1×130. A 2.5 mm entrance aperture was selected for optimal energy resolution, resulting in a collection semiangle of 16.8 mrad with the selected camera length of 37 mm. The energy resolution (full width at half maximum of the ZLP) of the EELS spectra was 90 meV. For plan-view spectrum imaging, a dwell time of 0.15 ms per pixel was used. For tilt-series spectrum imaging a dwell time of 0.1 ms per pixel was used.

For tilt-series EELS, spectrum images were acquired simultaneously with HAADF micrographs in a tilt series from 68° to −67° in 3° increments for electron tomography of the particle surface and in 9° increments for EELS.

Spectral Processing. Spectral processing was performed using HYPERSPY,[37] an open-source software coded in Python. An initial coarse alignment of the ZLP was performed, shifting the maximum intensity channel to zero, in order to define a reduced energy range and minimize the number of channels considered in subsequent processing. Then, spikes due to X-rays on the charge-coupled device detector were removed using a routine that automatically identified outlying high-intensity pixels and performed interpolation in the spectral region after removal of the spike. Spectra were subsequently aligned to the ZLP and cropped to the spectral region of interest (0.8 to 5 eV). For tilt-series data, the ZLP coarse alignment was retained and a subpixel alignment was performed only after concatenation of the tilt-series image stack in order to avoid multiple sequential subpixel interpolation steps. NMF decomposition was performed on plan-view and tilt-series spectrum images as reported previously.[22] NMF decomposition required a distinct component for the first pristine tilt (0°) for the lowest energy mode, attributed to a shift in the energy of the lowest energy resonance mode following acquisition of the first map and concomitant electron-beam-induced carbon contamination (see Figure S13). For surface charge reconstructions, the selected nonpenetrating trajectories were divided by the ZLP signal pixel-by-pixel to account for variation in the ZLP across the spectrum image (see also Supporting Information).

Surface Charge Reconstructions. The theoretical foundation and numerical demonstration of eigenmode surface charge reconstructions was reported by Hörl et al.[23] The reconstructions presented here used the nonlinear conjugate-gradient solver available in the open-source software SCIPY. In order to promote parsimonious solutions to the optimization

problem, eq 2 was modified with the addition of a regularization term to give

$$\hat{\sigma} = \arg\min_{\hat{\sigma}}\{\|\Gamma_n^{\mathrm{exp}}(\hat{\sigma}) - \Gamma_n^{\mathrm{calc}}(\hat{\sigma})\|_2^2 + \lambda\|F(\hat{\sigma})\|_2^2\} \quad (3)$$

where λ is a weighting factor and $F(\hat{\sigma})$ is an additional penalty term operating on the surface charge vector $\hat{\sigma}$.[38] In the case of corner modes, a few surface elements are highly charged and the remainder are near zero charge. As such, $F(\hat{\sigma})$ was selected as a soft thresholding operator to promote solutions of this kind:

$$\|F(\hat{\sigma})\|_2^2 = \sum_s \sigma_s^2 e^{-\gamma|\sigma_s|} \quad (4)$$

Only large charge density values are promoted in the solution by the regularization term (Figure S1), and so the total minimization scheme (eq 3) finds solutions consistent with the experimental data that also exhibit high surface charge values. Regularization parameters were selected by examining the effects of the weighting factors across a range of values to identify the minimum weighting required to remove spurious high-frequency surface charge oscillations from the reconstructions.

To implement the reconstruction procedure, a surface mesh of the particle was first reconstructed from HAADF electron tomography data using a compressed sensing reconstruction algorithm.[29] The volume was segmented, and a surface was extracted and meshed in AVIZO FIRE (FEI). A coordinate alignment was performed in MATLAB (Mathworks) using coordinate transformation and image registration routines. Reconstructions were initialized using the isolated particle eigenmodes calculated on the tomographically reconstructed particle surface. The use of simulated eigenmodes for the initialization of the reconstruction algorithm was noted to have a significant effect on the final reconstruction in phantom calculations comparing random and simulated initializations (see Figures S21−S23). The effect of contamination as a function of tilt was examined by comparison of simulated and experimental maps (see also Supporting Information). Additional validations of the presented reconstructions and method are presented in Figures S15−S23.

BEM Simulations. BEM simulations were performed using the open-source MNPBEM software.[39] The silver dielectric function was taken from ref 40. The MoO_3 refractive index was taken as 2.54 from ref 41. To model the effect of partial contamination resulting in red-shifted mode energies, an additional ambient dielectric constant of 1.5 was incorporated into simulations of the tomographically reconstructed bipyramid used for tilt-series EELS. For the simulations in Figure 1, the substrate was modeled as a 10 nm thick circular disk of 70 nm radius. An isolated bipyramid mesh was generated for initial BEM simulations of energy loss spectra (Figure S5). The mesh used for simulations in Figure 1 consisted of a total of 8011 surface elements with 2389 surface elements for the bipyramid surface (Figure S10). The mesh used for simulations in Figure 2 consisted of a total of 6000 surface elements with 2552 surface elements for the bipyramid surface (Figure S10) . The mesh used for eigenmode calculations of an isolated bipyramid presented in Figure 4 consisted of 6000 surface elements for the bipyramid surface (Figure S9).

ASSOCIATED CONTENT

Ⓢ Supporting Information

The Supporting Information is available free of charge on the ACS Publications website at DOI: 10.1021/acsphotonics.5b00421.

> Extended methods, additional discussion of NMF decomposition and BEM simulations, additional details on the validation of the reconstruction method, and reconstructions of edge and face modes (PDF)

AUTHOR INFORMATION

Corresponding Authors
*E-mail (S. M. Collins): smc204@cam.ac.uk.
*E-mail (P. A. Midgley): pam33@cam.ac.uk.

Notes
The authors declare no competing financial interest.

REFERENCES

(1) Anker, J. N.; Hall, W. P.; Lyandres, O.; Shah, N. C.; Zhao, J.; Van Duyne, R. P. Biosensing with plasmonic nanosensors. *Nat. Mater.* **2008**, 7, 442−453.

(2) Liu, N.; Hentschel, M.; Weiss, T.; Alivisatos, A. P.; Giessen, H. Three-Dimensional Plasmon Rulers. *Science* **2011**, 332, 1407−1410.

(3) Luk'yanchuk, B.; Zheludev, N. I.; Maier, S. A.; Halas, N. J.; Nordlander, P.; Giessen, H.; Chong, C. T. The Fano resonance in plasmonic nanostructures and metamaterials. *Nat. Mater.* **2010**, 9, 707−715.

(4) Deceglie, M. G.; Ferry, V. E.; Alivisatos, A. P.; Atwater, H. A. Design of Nanostructured Solar Cells Using Coupled Optical and Electrical Modeling. *Nano Lett.* **2012**, 12, 2894−2900.

(5) Batson, P. E. Surface Plasmon Coupling in Clusters of Small Spheres. *Phys. Rev. Lett.* **1982**, 49, 936−940.

(6) Prodan, E.; Radloff, C.; Halas, N. J.; Nordlander, P. A Hybridization Model for the Plasmon Response of Complex Nanostructures. *Science* **2003**, 302, 419−422.

(7) Sherry, L. J.; Chang, S.-H.; Schatz, G. C.; Van Duyne, R. P.; Wiley, B. J.; Xia, Y. Localized Surface Plasmon Resonance Spectroscopy of Single Silver Nanocubes. *Nano Lett.* **2005**, 5, 2034−2038.

(8) Ringe, E.; McMahon, J. M.; Sohn, K.; Cobley, C.; Xia, Y.; Huang, J.; Schatz, G. C.; Marks, L. D.; Van Duyne, R. P. Unraveling the Effects of Size, Composition, and Substrate on the Localized Surface Plasmon Resonance Frequencies of Gold and Silver Nanocubes: A Systematic Single-Particle Approach. *J. Phys. Chem. C* **2010**, 114, 12511−12516.

(9) Zhang, S.; Bao, K.; Halas, N. J.; Xu, H.; Nordlander, P. Substrate-Induced Fano Resonances of a Plasmonic Nanocube: A Route to Increased-Sensitivity Localized Surface Plasmon Resonance Sensors Revealed. *Nano Lett.* **2011**, 11, 1657−1663.

(10) Nelayah, J.; Kociak, M.; Stéphan, O.; García de Abajo, F. J.; Tencé, M.; Henrard, L.; Taverna, D.; Pastoriza-Santos, I.; Liz-Marzán,

L. M.; Colliex, C. Mapping surface plasmons on a single metallic nanoparticle. *Nat. Phys.* **2007**, *3*, 348−353.

(11) Rossouw, D.; Couillard, M.; Vickery, J.; Kumacheva, E.; Botton, G. A. Multipolar Plasmonic Resonances in Silver Nanowire Antennas Imaged with a Subnanometer Electron Probe. *Nano Lett.* **2011**, *11*, 1499−1504.

(12) Myroshnychenko, V.; Nelayah, J.; Adamo, G.; Geuquet, N.; Rodríguez-Fernández, J.; Pastoriza-Santos, I.; MacDonald, K. F.; Henrard, L.; Liz-Marzán, L. M.; Zheludev, N. I.; Kociak, M.; García de Abajo, F. J. Plasmon Spectroscopy and Imaging of Individual Gold Nanodecahedra: A Combined Optical Microscopy, Cathodoluminescence, and Electron Energy-Loss Spectroscopy Study. *Nano Lett.* **2012**, *12*, 4172−4180.

(13) Ringe, E.; Langille, M. R.; Sohn, K.; Zhang, J.; Huang, J.; Mirkin, C. A.; Van Duyne, R. P.; Marks, L. D. Plasmon Length: A Universal Parameter to Describe Size Effects in Gold Nanoparticles. *J. Phys. Chem. Lett.* **2012**, *3*, 1479−1483.

(14) Wiley, B. J.; Xiong, Y.; Li, Z.-Y.; Yin, Y.; Xia, Y. Right Bipyramids of Silver: A New Shape Derived from Single Twinned Seeds. *Nano Lett.* **2006**, *6*, 765−768.

(15) Ringe, E.; Zhang, J.; Langille, M. R.; Mirkin, C. A.; Marks, L. D.; Van Duyne, R. P. Correlating the structure and localized surface plasmon resonance of single silver right bipyramids. *Nanotechnology* **2012**, *23*, 444005.

(16) Zhang, W. C.; Wu, X. L.; Kan, C. X.; Pan, F. M.; Chen, H. T.; Zhu, J.; Chu, P. K. Surface-enhanced Raman scattering from silver nanostructures with different morphologies. *Appl. Phys. A: Mater. Sci. Process.* **2010**, *100*, 83−88.

(17) Tseng, W.-H.; Chiu, C.-Y.; Chou, S.-W.; Chen, H.-C.; Tsai, M.-L.; Kuo, Y.-C.; Lien, D.-H.; Tsao, Y.-C.; Huang, K.-Y.; Yeh, C.-T.; He, J.-H.; Wu, C.-I.; Huang, M. H.; Chou, P.-T. Shape-Dependent Light Harvesting of 3D Gold Nanocrystals on Bulk Heterojunction Solar Cells: Plasmonic or Optical Scattering Effect? *J. Phys. Chem. C* **2015**, *119*, 7554−7564.

(18) Perassi, E. M.; Hernandez-Garrido, J. C.; Moreno, M. S.; Encina, E. R.; Coronado, E. A.; Midgley, P. A. Using Highly Accurate 3D Nanometrology to Model the Optical Properties of Highly Irregular Nanoparticles: A Powerful Tool for Rational Design of Plasmonic Devices. *Nano Lett.* **2010**, *10*, 2097−2104.

(19) Perassi, E. M.; Hrelescu, C.; Wisnet, A.; Döblinger, M.; Scheu, C.; Jäckel, F.; Coronado, E. A.; Feldmann, J. Quantitative Understanding of the Optical Properties of a Single, Complex-Shaped Gold Nanoparticle from Experiment and Theory. *ACS Nano* **2014**, *8*, 4395−4402.

(20) García de Abajo, F.; Kociak, M. Probing the Photonic Local Density of States with Electron Energy Loss Spectroscopy. *Phys. Rev. Lett.* **2008**, *100*, 106804.

(21) Hohenester, U.; Ditlbacher, H.; Krenn, J. R. Electron-Energy-Loss Spectra of Plasmonic Nanoparticles. *Phys. Rev. Lett.* **2009**, *103*, 106801.

(22) Nicoletti, O.; de la Peña, F.; Leary, R. K.; Holland, D. J.; Ducati, C.; Midgley, P. A. Three-dimensional imaging of localized surface plasmon resonances of metal nanoparticles. *Nature* **2013**, *502*, 80−84.

(23) Hörl, A.; Trügler, A.; Hohenester, U. Tomography of Particle Plasmon Fields from Electron Energy Loss Spectroscopy. *Phys. Rev. Lett.* **2013**, *111*, 076801.

(24) von Cube, F.; Niegemann, J.; Irsen, S.; Bell, D. C.; Linden, S. Angular-resolved electron energy loss spectroscopy on a split-ring resonator. *Phys. Rev. B: Condens. Matter Mater. Phys.* **2014**, *89*, 115434.

(25) Li, G.; Cherqui, C.; Bigelow, N. W.; Duscher, G.; Straney, P. J.; Millstone, J. E.; Masiello, D. J.; Camden, J. P. Spatially Mapping Energy Transfer from Single Plasmonic Particles to Semiconductor Substrates via STEM/EELS. *Nano Lett.* **2015**, *15*, 3465−3471.

(26) Atre, A. C.; Brenny, B. J. M.; Coenen, T.; García-Etxarri, A.; Polman, A.; Dionne, J. A. Nanoscale optical tomography with cathodoluminescence spectroscopy. *Nat. Nanotechnol.* **2015**, *10*, 429−436.

(27) Dong, Z.; Bosman, M.; Zhu, D.; Goh, X. M.; Yang, J. K. W. Fabrication of suspended metal-dielectric-metal plasmonic nanostructures. *Nanotechnology* **2014**, *25*, 135303.

(28) García de Abajo, F. J.; Aizpurua, J. Numerical simulation of electron energy loss near inhomogeneous dielectrics. *Phys. Rev. B: Condens. Matter Mater. Phys.* **1997**, *56*, 15873−15884.

(29) Saghi, Z.; Holland, D. J.; Leary, R.; Falqui, A.; Bertoni, G.; Sederman, A. J.; Gladden, L. F.; Midgley, P. A. Three-Dimensional Morphology of Iron Oxide Nanoparticles with Reactive Concave Surfaces. A Compressed Sensing-Electron Tomography (CS-ET) Approach. *Nano Lett.* **2011**, *11*, 4666−4673.

(30) Collins, S. M.; Nicoletti, O.; Rossouw, D.; Ostasevicius, T.; Midgley, P. A. Excitation dependent Fano-like interference effects in plasmonic silver nanorods. *Phys. Rev. B: Condens. Matter Mater. Phys.* **2014**, *90*, 155419.

(31) McClain, M. J.; Schlather, A. E.; Ringe, E.; King, N. S.; Liu, L.; Manjavacas, A.; Knight, M. W.; Kumar, I.; Whitmire, K. H.; Everitt, H. O.; Nordlander, P.; Halas, N. J. Aluminum Nanocrystals. *Nano Lett.* **2015**, *15*, 2751−2755.

(32) Brintlinger, T.; Herzing, A. A.; Long, J. P.; Vurgaftman, I.; Stroud, R.; Simpkins, B. S. Optical Dark-Field and Electron Energy Loss Imaging and Spectroscopy of Symmetry-Forbidden Modes in Loaded Nanogap Antennas. *ACS Nano* **2015**, *9*, 6222−6232.

(33) Guiton, B. S.; Iberi, V.; Li, S.; Leonard, D. N.; Parish, C. M.; Kotula, P. G.; Varela, M.; Schatz, G. C.; Pennycook, S. J.; Camden, J. P. Correlated Optical Measurements and Plasmon Mapping of Silver Nanorods. *Nano Lett.* **2011**, *11*, 3482−3488.

(34) Boudarham, G.; Kociak, M. Modal decompositions of the local electromagnetic density of states and spatially resolved electron energy loss probability in terms of geometric modes. *Phys. Rev. B: Condens. Matter Mater. Phys.* **2012**, *85*, 245447.

(35) Losquin, A.; Zagonel, L. F.; Myroshnychenko, V.; Rodríguez-González, B.; Tencé, M.; Scarabelli, L.; Förstner, J.; Liz-Marzán, L. M.; García de Abajo, F. J.; Stéphan, O.; Kociak, M. Unveiling Nanometer Scale Extinction and Scattering Phenomena through Combined Electron Energy Loss Spectroscopy and Cathodoluminescence Measurements. *Nano Lett.* **2015**, *15*, 1229−1237.

(36) Zhang, Q.; Cobley, C.; Au, L.; McKiernan, M.; Schwartz, A.; Wen, L.-P.; Chen, J.; Xia, Y. Production of Ag Nanocubes on a Scale of 0.1 g per Batch by Protecting the NaHS-Mediated Polyol Synthesis with Argon. *ACS Appl. Mater. Interfaces* **2009**, *1*, 2044−2048.

(37) de la Peña, F.; Berger, M.-H.; Hochepied, J.-F.; Dynys, F.; Stéphan, O.; Walls, M. Mapping titanium and tin oxide phases using EELS: An application of independent component analysis. *Ultramicroscopy* **2011**, *111*, 169−176.

(38) Calvetti, D.; Morigi, S.; Reichel, L.; Sgallari, F. Tikhonov regularization and the L-curve for large discrete ill-posed problems. *Journal of Computational and Applied Mathematics* **2000**, *123*, 423−446.

(39) Hohenester, U. Simulating electron energy loss spectroscopy with the MNPBEM toolbox. *Comput. Phys. Commun.* **2014**, *185*, 1177−1187.

(40) Johnson, P. B.; Christy, R. W. Optical Constants of the Noble Metals. *Phys. Rev. B* **1972**, *6*, 4370−4379.

(41) Deb, S. K. Physical Properties of a Transition Metal Oxide: Optical and Photoelectric Properties of Single Crystal and Thin Film Molybdenum Trioxide. *Proc. R. Soc. London, Ser. A* **1968**, *304*, 211−231.